Semianalytical modeling of squirrel-cage induction machines with consideration of iron permeability and eddy-currents using elementary subdomain technique

Lazhar Roubache, Kamel Boughrara, Frédéric Dubas, Brahim Ladghem-Chikouche, Rachid Ibtiouen

DOI: 10.1108/COMPEL-06-2023-0219, COMPEL – The International Journal for Computation and Mathematics in Electrical and Electronic Engineering

Semi-analytical modeling of squirrel-cage induction machines with consideration of iron permeability and eddy-currents using elementary subdomain technique

Lazhar Roubache[1], Kamel Boughrara[2], Frédéric Dubas[3], Brahim Ladghem Chikouche[2] and Rachid Ibtiouen[2]

[1]Laboratoire Des Sciences Appliquées, Ecole National Supérieure des Technologies Avancées, Alger, Algeria
[2]Laboratoire de Recherche en Electrotechnique (LRE-ENP), Ecole Nationale Polytechnique, Alger, Algeria
[3]Département ENERGIE, FEMTO-ST, CNRS, Univ. Bourgogne Franche-Comté, Belfort, France

ABSTRACT

Purpose – In this article, the authors present a semi-analytical model of a squirrel-cage induction machine (SCIM), considering local magnetic saturation and eddy-currents induced in the rotor bars.

Design/methodology/approach – The regions of the rotor and stator are divided into elementary subdomains (E-SDs) characterized by general solutions at the first harmonic of the magneto-harmonic Maxwell's equations. These E-SDs are connected in both directions (i.e., along the r-and θ-edges).

Findings – The calculation of the magnetic field has been validated for various values of slip and iron permeability. All electromagnetic quantities were compared to those obtained using a two-dimensional (2-D) finite-element method (FEM). The semi-analytical results are satisfactory compared to the numerical results, considering both the amplitude and waveform.

Originality/value – Expansion of the recent analytical model (E-SD technique) for the full prediction of the magnetic field in SCIMs, considering the local saturation effect and the eddy-currents induced in the rotor bars.

Keywords Magnetic field, Analytical methods, Induction machines, Eddy-currents, Elementary subdomain technique, Electromagnetic performances.

Paper type Research paper.

1. INTRODUCTION:

Induction machines (IM) find diverse applications in industrial and domestic sectors, emphasizing the importance of enhancing electric device performance and minimizing energy consumption. While the finite-element method (FEM) is commonly employed for studying electric machine design, its use in optimal design can be time-consuming. On the contrary, semi-analytical models offer a fast, accurate, and particularly suitable alternative for the early stages of optimal design. The subdomain (SD) technique stands out as an efficient semi-analytical method for computing the magnetic field in electrical machines. Several state-of-the-art studies on this technique in electric machines can be found in (Devillers, et al., 2016), (Tiegna, et al., 2013) and (Dubas & Boughrara, 2017a). The application of this modeling to squirrel-cage induction machines (SCIMs) can be found in (Roubache, et al., 2016), (Boughrara, et al., 2014), (Lubin, et al., 2011) and (Sprangers, et al., 2014). However, these research studies neglect the saturation effect in iron parts. Magnetic circuit saturation significantly influences machine inductance, torque ripple, power factor, and efficiency. Therefore, the consideration of saturation is crucial for accurately predicting machine performance. Various approaches have been proposed to model the magnetic saturation effect in IMs. In (Moulahoum, et al., 2007) and (Aller, et al., 2013), defined coefficients based on the flux linkage of the machine were added to the equivalent circuit approach to modulate magnetic saturation. The air-gap saturation flux harmonics are used in (Tu, et al., 2008) to predict the magnetization level. In (Mollaeian, et al., 2021), the authors used Fourier-based modeling considering finite permeability to model magnetic saturation in IM. Recent work has focused on the calculation of the magnetic field inside the machine considering the magnetic saturation effects (Roshandel, et al., 2020) and (Roshandel, et al., 2022). The authors proposed a coupled model based on electric equivalent circuit (EEC) and SD technique with magnetostatic formulation. The EEC parameters were calculated using magnetic vector potentials obtained from the SD model. A similar approach has been proposed in (Sapmaz & Oner, 2022). The model combines the magnetic equivalent circuit and SD technique to calculate electromagnetic performance of IMs considering steel permeability. In this paper, we proposed a direct consideration of the local saturation effect in the calculation of the magnetic field using the SD technique.

A new scientific contribution to the SD technique is proposed in (Dubas & Boughrara, 2017a) and (Dubas & Boughrara, 2017b) by incorporating ferromagnetic regions. The general solution of the 2-D magneto static field equations is decomposed into a Fourier series based on two solutions in both directions. The interface conditions (ICs) on different edges are then satisfied through the application of the principle of superposition. This methodology was implemented on radial flux electric machines with permanent-

magnets in (Roubache, et al., 2018). In (Roubache, et al., 2019), the authors developed a semi-analytical model with local magnetic saturation using the iterative Newton-Raphson (NR) algorithm. The main idea of this innovative model is to mesh the rotor and stator regions into elementary subdomains (E-SDs). While the general solution remains consistent with that in (Roubache, et al., 2018), the E-SDs are assumed to be small enough for the variation of the magnetic vector potential to be considered insignificant. Thus, only the first harmonics in the r and θ directions are considered in the general solution.

In this paper, the authors proposed semi-analytical modeling of a SCIM in magneto-harmonic formulation using the E-SDs technique. The model accounts for the effect of local magnetic saturation and considers the eddy-currents induced in the rotor bars. By assuming sufficiently small E-SDs, the estimation of eddy-currents in the rotor bars becomes feasible. The proposed model is utilized to simulate SCIM for various values of relative permeability and slip. The 2-D semi-analytical results are then compared with those obtained using FEMM (Meeker, 2009).

2. MATHEMATICAL FORMULATION IN E-SDs

2.1. Assumptions

The proposed model is formulated in magnetic vector potential **A** with the following assumptions:

- the end-effects are neglected (i.e., that the magnetic variables are independent of z);
- the stator slots/teeth and the rotor slots/teeth have radial sides;
- the current density has only one component along the z-axis;
- except rotor bars, the electrical conductivities of materials are assumed to be null;
- the E-SDs are considered as isotropic regions;
- the iron reluctivity is a function of the mean value of the magnetic field **B** in each E-SD.

2.2.Mesh generation and magnetic field solution

The main concept of the proposed model involves partitioning the regions of the machine into E-SDs. The general solution of Maxwell's equations is then employed, following the approach in (Roubache, et al., 2019), where only the first radial and tangential components are considered. However, the solutions within the E-SDs corresponding to the rotor bars are modified to account for the eddy-currents.

Figure 1 illustrates a SCIM with the identification of various regions, while **Figure 2** shows the meshing of the rotor and stator regions using E-SDs.

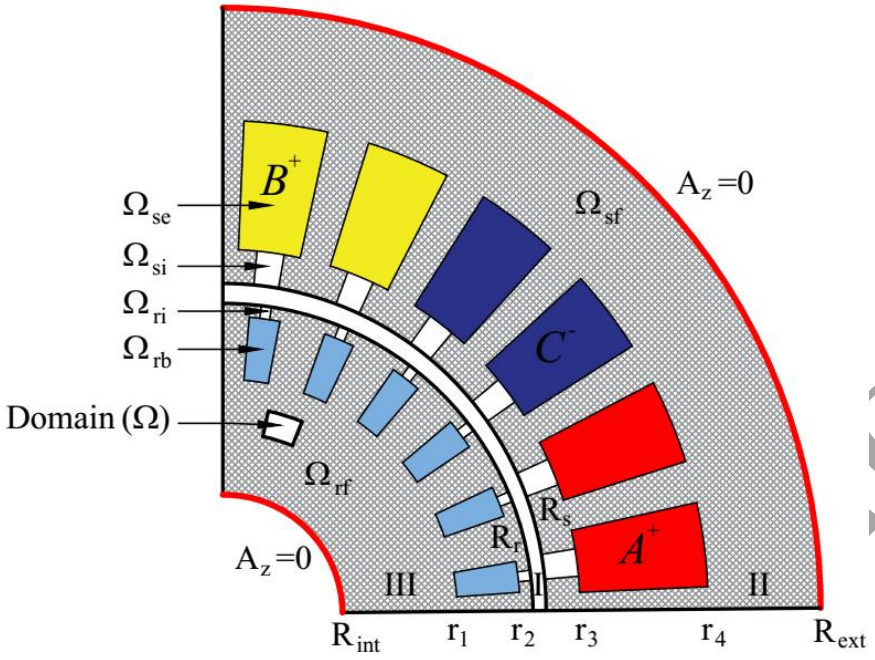

Figure 1: Squirrel-cage induction machine

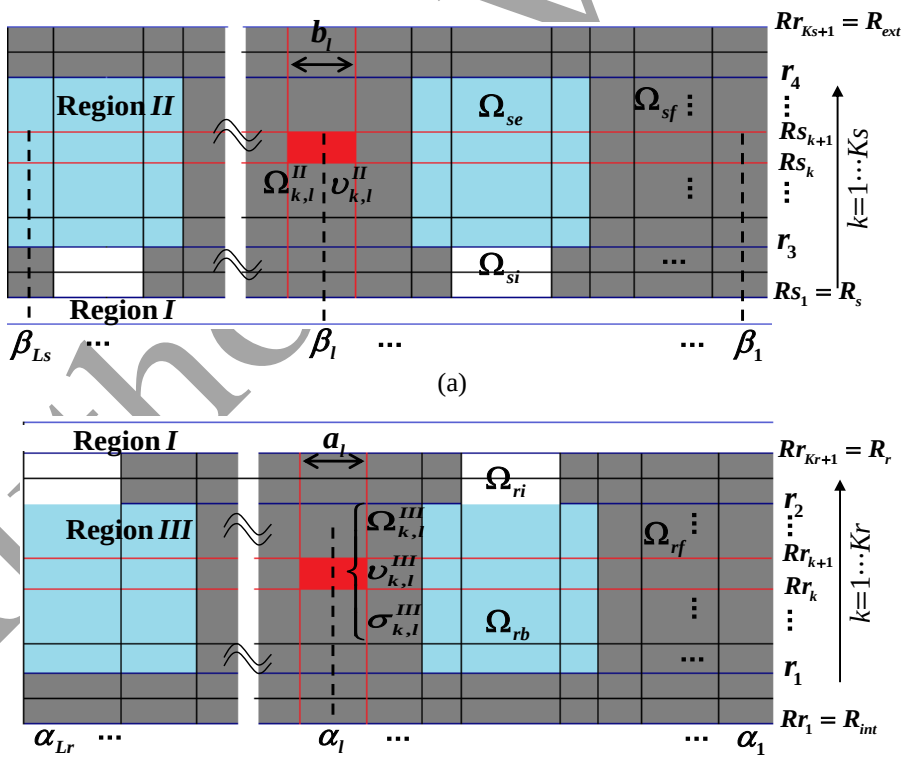

Figure 2: Mesh in E-SDs of: (a) stator and (b) rotor

In the magneto-harmonic model, the magnetic vector potential is expressed as follows:

$$A_z(r,\theta,t) = \Re e\left\{A_z(r,\theta)\cdot e^{j\omega\cdot t}\right\} \text{ in the air-gap \& the stator} \quad (1)$$

$$A_z(r,\theta,t) = \Re e\left\{ A_z(r,\theta) \cdot e^{\boldsymbol{j}\omega_{rm} \cdot t} \right\} \text{ with } \omega_{rm} = s\omega = \omega - p\varpi_r \text{ in the rotor} \quad (2)$$

where $\boldsymbol{j} = \sqrt{-1}$, ω_{rm} is the electrical pulsation at the rotor, *s* is the slip, ω is the electrical pulsation at the stator, *p* is the number of pole pairs, and ϖ_r is the angular speed of the rotor.

The partial differential equation derived from Maxwell's equations for each subdomain Ω is expressed as follows:

$$\Delta A_z = \boldsymbol{j}\mu_0 \sigma \omega_{rm} A_z \text{ for } \Omega \in \Omega_{rb}^j \quad (3)$$

$$\Delta A_z = -\mu_0 \cdot J_{sz}^i \text{ for } \Omega \in \Omega_{se}^i \quad (4)$$

$$\Delta A_z = 0 \text{ for } \Omega \in \Omega_{rf} \cup \Omega_{sf} \cup \Omega_{si} \cup \Omega_{ri} \cup \Omega_I \quad (5)$$

where J_{sz}^i is the current density in the i[th] stator slot, σ is the conductivity of the rotor bars, Ω_{se}^i & Ω_{rb}^j are respectively the i[th] stator slot and the j[th] rotor bar, Ω_{rf} & Ω_{sf} are the regions of iron, Ω_{ri} & Ω_{si} are respectively the slot-openings in the rotor and in the stator, and Ω_I is the air-gap region (Region I).

The solution of the Helmholtz equation **(3)** in the rotor bars results in Bessel functions in the radial direction (Roubache, et al., 2016). However, these functions are non-periodic and unsuitable for connecting the E-SDs at the *r*-edges. Since the E-SDs are sufficiently small, the variation of $A_z^{\Omega_{rb}}$ can be considered insignificant. This consideration leads to only considering the first harmonics according in the *r* and θ direction. Furthermore, we can assume that the eddy-currents induced in each E-SD, which belong to the rotor bars, are constant. Therefore, **(3)** can be simplified to:

$$\Delta A_z = -\mu_0 \cdot J_{rz}^j \text{ for } \Omega \in \Omega_{Rb}^j \quad (6)$$

$$J_{rz}^j(r,\theta) \approx J_{rz}^j = -\boldsymbol{j}\sigma\omega_{rm} \cdot \overline{A}_z \quad (7)$$

where $\overline{A}_z$ is the mean value of A_z in $\Omega \in \Omega_{Rb}^j$.

The formulation presented in this paper necessitates defining the mesh elements illustrated in **Figure 2**

$$\alpha = \begin{bmatrix} \alpha_1 & \cdots & \alpha_l & \cdots & \alpha_{Lr} \end{bmatrix} \in \Re^{Lr \times 1} \quad (8)$$

$$a = \begin{bmatrix} a_1 & \cdots & a_l & \cdots & a_{Lr} \end{bmatrix} \in \Re^{Lr \times 1} \quad (9)$$

$$\beta = \begin{bmatrix} \beta_1 & \cdots & \beta_l & \cdots & \beta_{Ls} \end{bmatrix} \in \Re^{Ls \times 1} \quad (10)$$

$$b = \begin{bmatrix} b_1 & \cdots & b_l & \cdots & b_{Ls} \end{bmatrix} \in \Re^{Ls \times 1} \quad (11)$$

$$Rr = \begin{bmatrix} R_{\text{int}} & \cdots & Rr_k & \cdots & Rr_{Kr+1} \end{bmatrix} \in \Re^{(Kr+1) \times 1} \quad (12)$$

$$Rs = \begin{bmatrix} R_s & \cdots & Rs_k & \cdots & Rs_{Ks+1} \end{bmatrix} \in \Re^{(Ks+1)\times 1} \tag{13}$$

$$\upsilon_{II} = \left\{ \upsilon_{II}^{k,l} \right\} \in \Re^{Ks \times Ls} \tag{14}$$

$$J_{z\,II} = \left\{ J_{II}^{k,l} \right\} \in \Re^{Ks \times Ls} \tag{15}$$

$$\upsilon_{III} = \left\{ \upsilon_{III}^{k,l} \right\} \in \Re^{Kr \times Lr} \tag{16}$$

$$\sigma_{III} = \left\{ \sigma_{III}^{k,l} \right\} \in \Re^{Kr \times Lr} \tag{17}$$

with

$$\upsilon_{II}^{k,l} = \begin{cases} \dfrac{1}{\mu_0} & \text{if } \Omega_{k,l}^{II} \in \Omega_{sf} \bigcup \Omega_{si} \\ \dfrac{1}{\mu_r \mu_0} & \text{if } \Omega_{k,l}^{II} \in \Omega_{sf} \end{cases} \tag{18}$$

$$J_{II}^{k,l} = \begin{cases} 0 & \text{if } \Omega_{k,l}^{II} \in \Omega_{sf} \bigcup \Omega_{si} \\ J_{sz}^{i} & \text{if } \Omega_{k,l}^{II} \in \Omega_{se}^{i} \end{cases} \tag{19}$$

$$\upsilon_{III}^{k,l} = \begin{cases} \dfrac{1}{\mu_0} & \text{if } \Omega_{k,l}^{III} \in \Omega_{rb} \bigcup \Omega_{ri} \\ \dfrac{1}{\mu_r \mu_0} & \text{if } \Omega_{k,l}^{III} \in \Omega_{rf} \end{cases} \tag{20}$$

$$\sigma_{III}^{k,l} = \begin{cases} 0 & \text{if } \Omega_{k,l}^{III} \in \Omega_{rf} \bigcup \Omega_{ri} \\ \sigma & \text{if } \Omega_{k,l}^{III} \in \Omega_{rb} \end{cases} \tag{21}$$

The solution of **(4)** ~ **(6)** are defined for each region as follows (Dubas & Boughrara, 2017b):

- In the air-gap (**Region I**):

$$\begin{aligned} A_{z\,I}(r,\theta) = A1_0 + A2_0 \ln(r) + \sum_{n=1}^{\infty} \left[A1_n \left(\frac{r}{R_s} \right)^n + A2_n \left(\frac{r}{R_r} \right)^{-n} \right] sin(n\theta) \\ \cdots + \sum_{n=1}^{\infty} \left[A3_n \left(\frac{r}{R_s} \right)^n + A4_n \left(\frac{r}{R_r} \right)^{-n} \right] cos(n\theta) \end{aligned} \tag{22}$$

where $\left\{ A1_0; A2_0; A1_n \sim A4_n \right\}$ are the integration constants in the air-gap, and *n* the spatial harmonics.

- In the stator (**Region II**)

$$A_{z\,II}^{k,l} = C_1^{k,l} + C_2^{k,l}\ln(r) - \frac{1}{4}\mu_0 J_{II}^{k,l} r^2 + \left(C_3^{k,l} r^{\vartheta_{sl}} + C_4^{k,l} r^{-\vartheta_{sl}}\right)\cos\left[\vartheta_{sl}\left(\theta - \beta_l + \frac{b_l}{2}\right)\right] \\ \cdots + \left\{C_5^{k,l}\sinh\left[\lambda_{sk}\left(\theta - \beta_l + \frac{b_l}{2}\right)\right] + C_6^{k,l}\sinh\left[\lambda_{sk}\left(\theta - \beta_l - \frac{b_l}{2}\right)\right]\right\}\sin\left[\lambda_{sk}\ln\left(\frac{r}{Rs_k}\right)\right] \tag{23}$$

with

$$\lambda_{sk} = \frac{\pi}{\ln\left(Rs_{k+1}/Rs_k\right)} \;\&\; \vartheta_{sl} = \frac{\pi}{b_l} \tag{24}$$

where $\left\{C_1^{k,l} \sim C_6^{k,l}\right\}$ are the integration constants in the stator.

- In the rotor (**Region III**)

According to **(6)**, the general solution in the rotor can be defined by

$$A_{z\,III}^{k,l} = B_1^{k,l} + B_2^{k,l}\ln(r) - \frac{1}{4}\mu_0 J_{z\,III}^{k,l} r^2 + \left(B_3^{k,l} r^{\vartheta_{rl}} + B_4^{k,l} r^{-\vartheta_{rl}}\right)\cos\left[\vartheta_{rl}\left(\theta - \alpha_l + \frac{a_l}{2}\right)\right] \\ \cdots + \left\{B_5^{k,l}\sinh\left[\lambda_{rk}\left(\theta - \alpha_l + \frac{a_l}{2}\right)\right] + B_6^{k,l}\sinh\left[\lambda_{rk}\left(\theta - \alpha_l - \frac{b_l}{2}\right)\right]\right\}\sin\left[\lambda_{rk}\ln\left(\frac{r}{Rr_k}\right)\right] \tag{25}$$

with

$$\lambda_{rk} = \frac{\pi}{\ln\left(Rr_{k+1}/Rr_k\right)} \;\&\; \vartheta_{rl} = \frac{\pi}{a_l} \tag{26}$$

yet, $J_{z\,III}^{k,l} = -\boldsymbol{j}\sigma_{III}^{k,l}\omega_{rm}\cdot\overline{A}_{z\,III}^{k,l}$ which give

$$J_{z\,III}^{k,l} = -\boldsymbol{j}\sigma_{III}^{k,l}\omega_{rm}\left[B_1^{k,l} + \xi_2^{k,l}B_2^{k,l} - \gamma_{k,l}J_{z\,III}^{k,l} + \xi_5^{k,l}\left(B_5^{k,l} - B_6^{k,l}\right)\right] \tag{27}$$

with

$$\gamma_{k,l} = \mu_0\left(Rr_{k+1}^2 + Rr_k^2\right)/8 \tag{28}$$

$$\xi_2^{k,l} = \frac{a_l\left[Rr_{k+1}^2\ln\left(Rr_{k+1}\right) - Rr_k^2\ln\left(Rr_k\right)\right]}{2\,S_{\Omega_{k,l}^{III}}} - \frac{1}{2} \tag{29}$$

$$\xi_5^{k,l} = Rr_k^2\,\frac{\left[\cosh\left(\lambda_{rk}a_l\right) - 1\right]\left[e^{2\ln\left(Rr_{k+1}/Rr_k\right)} + 1\right]}{S_{\Omega_{k,l}^{III}}\left(4 + \lambda_{rk}^2\right)} \tag{30}$$

and $S_{\Omega_{k,l}^{III}} = a_l\left(Rr_{k+1}^2 - Rr_k^2\right)/2$ represents the area of $\Omega_{k,l}^{III}$

Finally, by using **(27)** ~ **(30)**, **(25)** becomes

$$\begin{aligned} A_{z\,III}^{k,l} &= B_1^{k,l} + B_2^{k,l}\ln(r) + \chi^{k,l}\left(B_1^{k,l} + \xi_2^{k,l}B_2^{k,l} + \xi_5^{k,l}\left(B_5^{k,l} - B_6^{k,l}\right)\right)r^2 \\ &\cdots + \left(B_3^{k,l}r^{\vartheta_{rl}} + B_4^{k,l}r^{-\vartheta_{rl}}\right)\cos\left[\vartheta_{rl}\left(\theta - \alpha_l + \frac{a_l}{2}\right)\right] \\ &\cdots + \left\{B_5^{k,l}\sinh\left[\lambda_{rk}\left(\theta - \alpha_l + \frac{a_l}{2}\right)\right] + B_6^{k,l}\sinh\left[\lambda_{rk}\left(\theta - \alpha_l - \frac{a_l}{2}\right)\right]\right\}\sin\left[\lambda_{rk}\ln\left(\frac{r}{Rr_k}\right)\right] \end{aligned} \tag{31}$$

with

$$\chi^{k,l} = \frac{\boldsymbol{j}\sigma_{II}^{k,l}\omega_{rm}\mu_0}{4\left(1 - \boldsymbol{j}\sigma_{II}^{k,l}\omega_{rm}\gamma_{k,l}\right)} \tag{32}$$

where $\left\{B_1^{k,l} \sim B_6^{k,l}\right\}$ are the integration constants in the rotor.

2.3. Performing of the interface conditions (ICs)

By considering the ICs between the various domains and regions, it becomes possible to determine the integration constants in **(22)**, **(23)** and **(31)** through the solution of the following system of linear equations:

$$M \cdot X = Y \tag{33}$$

with

$$M = \begin{bmatrix} \Lambda^{11} & \Lambda^{12} & \Lambda^{13} \\ 0 & \Lambda^{22} & 0 \\ 0 & 0 & \Lambda^{33} \\ \Lambda^{41} & \Lambda^{42}\left(\upsilon_{III}^{k,l}\right) & \Lambda^{43}\left(\upsilon_{II}^{k,l}\right) \\ 0 & \Lambda^{52}\left(\upsilon_{III}^{k,l}\right) & 0 \\ 0 & 0 & \Lambda^{63}\left(\upsilon_{II}^{k,l}\right) \end{bmatrix} \tag{34}$$

$$X = \begin{bmatrix} \mathrm{a}^{air} & b^{rotor} & c^{stator} \end{bmatrix}^T \tag{35}$$

$$Y = \begin{bmatrix} \Gamma^1 & \Gamma^2 & \Gamma^3 & \Gamma^4 & \Gamma^5 & \Gamma^6 \end{bmatrix} \tag{36}$$

$$\mathrm{a}^{air} = \begin{bmatrix} A1_0 \cdots A1_N & A2_0 \cdots A2_N & A3_1 \cdots A3_N & A4_1 \cdots A4_N \end{bmatrix} \in \Re^{(4N+2)\times 1} \tag{37}$$

$$b^{rotor} = \begin{bmatrix} B_1^{1,1} \cdots B_6^{1,1} & B_1^{1,2} \cdots B_6^{1,2} & \cdots & B_1^{K_r,L_r} \cdots B_6^{K_r,L_r} \end{bmatrix} \in \Re^{(6K_rL_r)\times 1} \tag{38}$$

$$c^{stator} = \left[C_1^{1,1} \cdots C_6^{1,1} \; C_1^{1,2} \cdots C_6^{1,2} \; \cdots C_1^{K_s,L_s} \cdots C_6^{K_s,L_s} \right] \in \Re^{(6K_sL_s)\times 1} \tag{39}$$

The development of these ICs and submatrices can be referenced in (Roubache, et al., 2019).

2.4. Newton Raphson's (NR's) Iterative Algorithm

The integration constants in **(33)** (i.e., vector X) can be determined by solving the following system of nonlinear equations obtained from the ICs between the various regions.

$$f(X) = \left[M(X) \right] X + Y = 0 \tag{40}$$

It is important to note that $\left\{ \Lambda^{11}; \Lambda^{12}; \Lambda^{13}; \Lambda^{22}; \Lambda^{33} \right\}$, corresponding to the ICs of A_z, remains unaffected by the reluctivity of the materials. On the other hand, the remaining submatrices correspond to the ICs of $H_{//}$, which depend on the reluctivity of the materials and are also related to the unknowns' vector X.

The Jacobian matrix of $f(X)$ can be written for the k^{th} iteration as

$$J^k(X^k) = \left[M(X^k) \right] + \left[\Lambda \right] X^k \tag{41}$$

where

$$\left[\Lambda \right] = \begin{bmatrix} 0 & 0 & 0 \\ 0 & 0 & 0 \\ 0 & 0 & 0 \\ 0 & \partial \Lambda^{42} / \partial b^{rotor} & \partial \Lambda^{43} / \partial c^{stator} \\ 0 & \partial \Lambda^{52} / \partial b^{rotor} & 0 \\ 0 & 0 & \partial \Lambda^{63} / \partial b^{stator} \end{bmatrix} \tag{42}$$

The solutions of magnetic vector potential in iron regions (i.e., Ω_{rf} & Ω_{sf}) have the same form as in the case of magnetostatic study. Moreover, the Jacobian matrix is independent of the integration constants of the other regions. Therefore, the description of $\left[\Lambda \right]$ and the NR's iterative formula can be found in (Roubache, et al., 2019). **Figure 3** shows the flowchart for calculating electromagnetic performance.

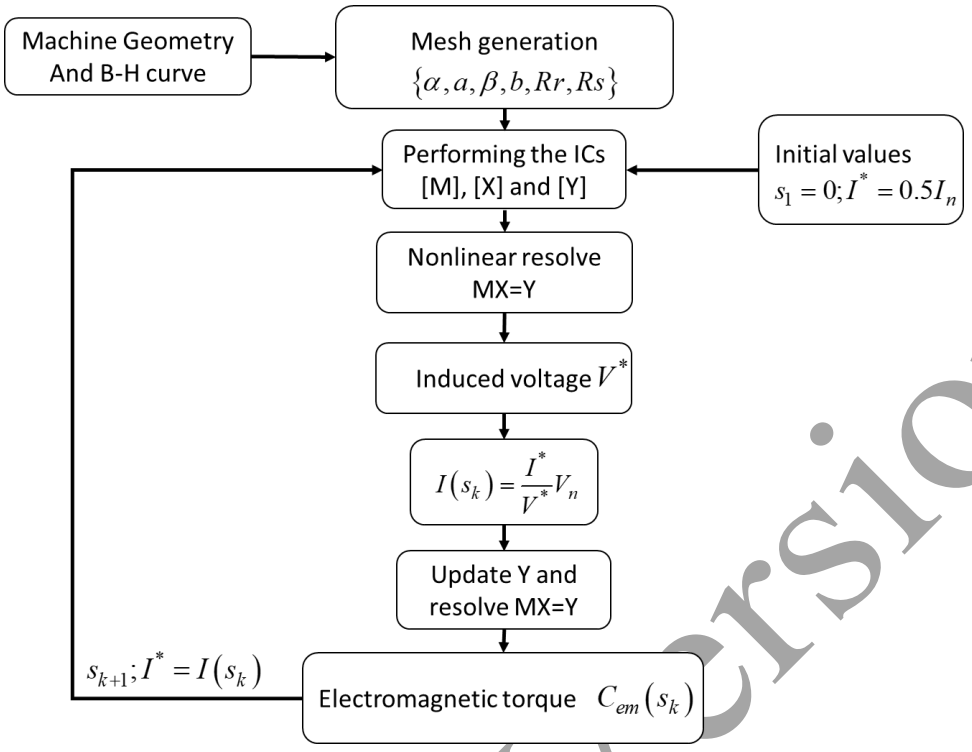

Figure 3 : Flowchart for calculating electromagnetic performance

3. RESULTS AND VALIDATIONS

3.1. Electromagnetic performances

The developed semi-analytical model is used to determine the magnetic field in all regions of the SCIM, as well as the surface density of eddy-currents induced in the rotor bars and the electromagnetic torque. The geometric and physical parameters of the machine are detailed in **Table 1** .

Figures 4~6 illustrate the various components of magnetic flux density in the middle of the air-gap for different values of the relative permeability of iron and slip (i.e., $\{\mu_r; s\} = \{100; 0.1\}, \{600; 0.1\}, \{600; 1\}$). The semi-analytical results exhibit a strong agreement with the numerical results concerning both amplitude and waveform. The amplitude gradient of the magnetic flux density and magnetic vector potential inside the SCIM for $\{\mu_r; s\} = \{600; 0.1\}$ are respectively illustrated in **Figures 7-8**.

Figures 9-10 represent the eddy-currents induced in the rotor bars obtained analytically and numerically for $\{\mu_r; s\} = \{600; 0.1\}, \{600; 1\}$. The semi-analytical results demonstrate a high level of agreement with the numerical results.

Table 1 : Geometrical and physical parameters of the SCIM

Symbol	Parameters	Value
I_m	Peak phase current	18 *A*
V_m	Peak phase voltage	220 V
P_n	Nominal power	3 kW
N_n	Nominal speed	1,425 rpm
s_n	Nominal slip	5%
N_c	Number of conductors per stator slot	60
σ	Electrical conductivity of rotor bars	35 MS/m
Q_s	Number of stator slots	24
c	Stator slot-opening	7.5 *deg.*
c_r	Stator isthmus-opening	2.5 *deg.*
a	Rotor slot-opening	5.45 *deg.*
a_r	Rotor isthmus-opening	1.9 *deg.*
p	Number of pole pairs	2
R_{ext}	Radius of the external stator surface	95 *mm*
r_4	External radius of stator slot	83 *mm*
r_3	Internal radius of stator slot	63 *mm*
R_s	Radius of the internal stator surface	61 *mm*
R_r	Radius of the external rotor surface	60 *mm*
r_2	External radius of rotor bars	58 *mm*
r_1	Internal radius of rotor bars	48 *mm*
$R_{int\ t}$	Radius of the rotor inner surface	20 *mm*
G	Air-gap thickness	1 *mm*
L_u	Axial length	63 *mm*

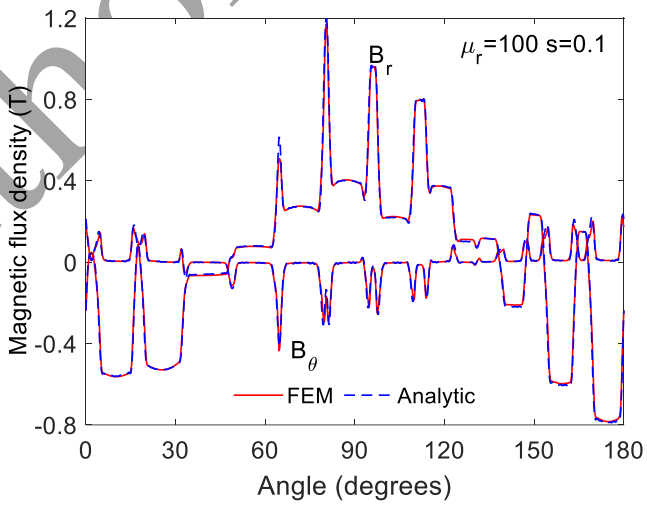

Figure 4 : Waveform of *r*- and *θ*-component of B in the middle of the air-gap for $\mu_r = 100$ and $s = 0.1$

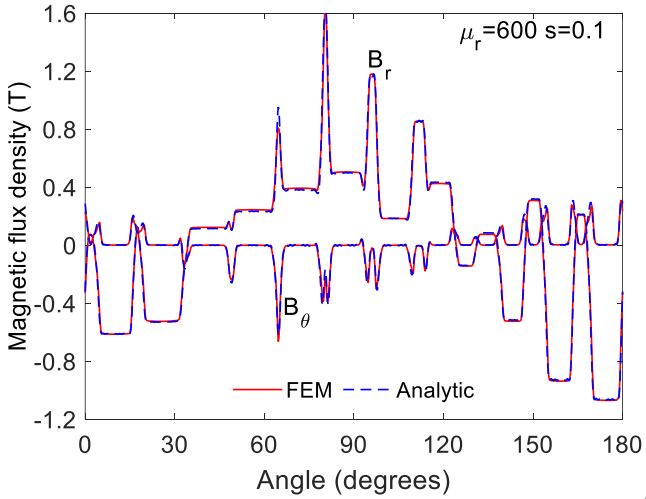

Figure 5 : Waveform of *r*- and *θ*-component of B in the middle of the air-gap for μ_r = *600* and *s* = *0.1*

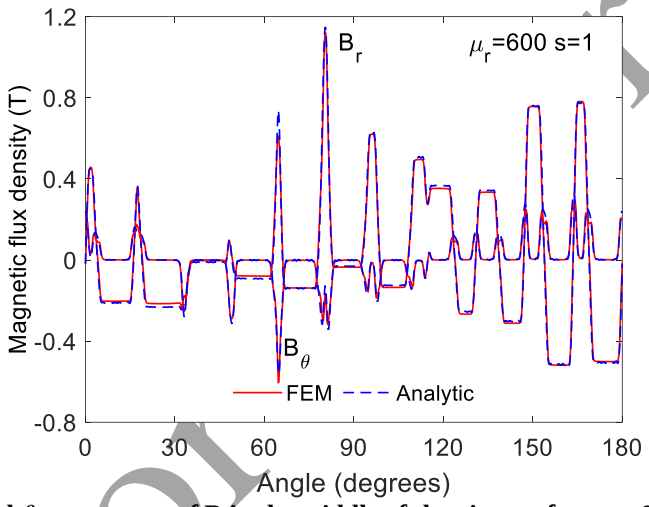

Figure 6 : Waveform of *r*- and *θ*-component of B in the middle of the air-gap for μ_r = *600* and *s* = *1*

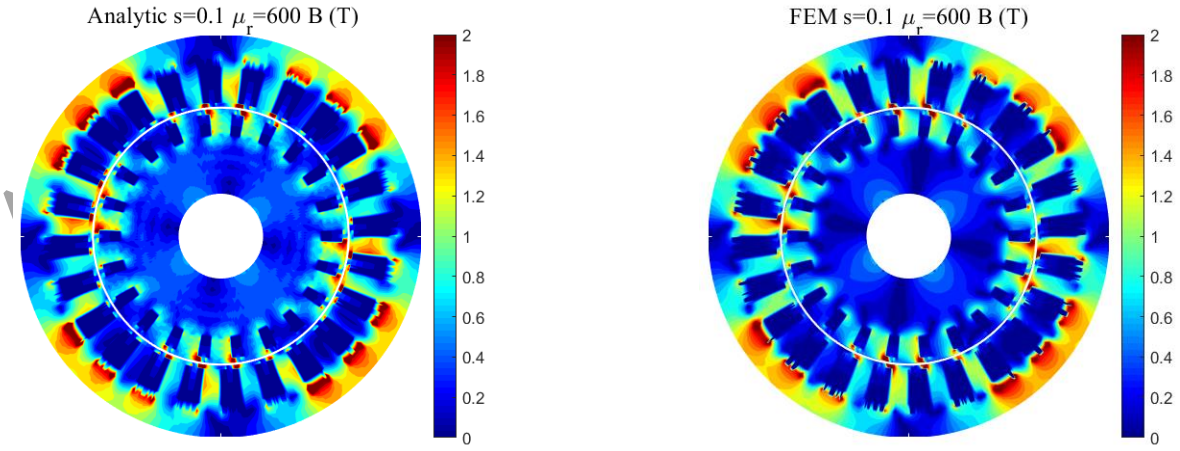

(a) (b)

Figure 7 : Magnetic flux density inside the SCIM for μ_r = *600* and *s* = *0.1* : (a) analytic and (b) FEM

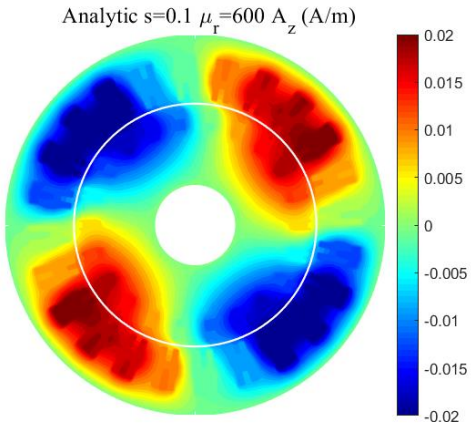

(a)

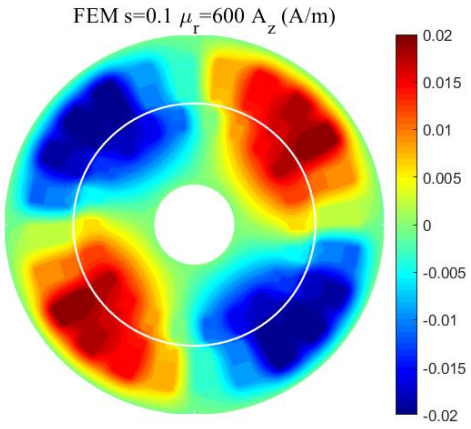

(b)

Figure 8 : Magnetic vector potential inside the SCIM for μ_r = 600 and s = 0.1 : (a) analytic and (b) FEM

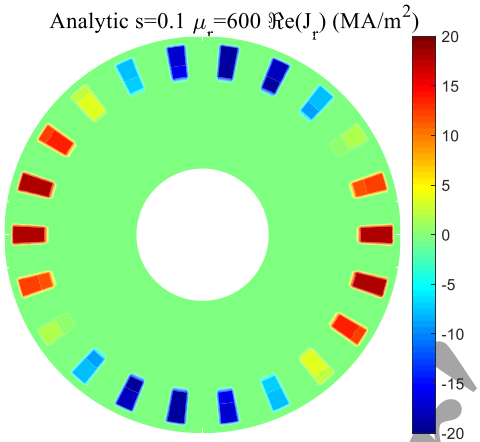

(a)

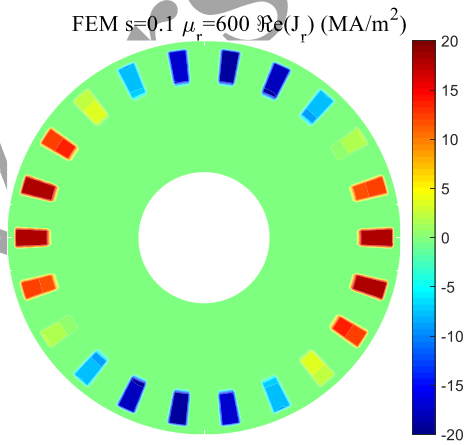

(b)

Figure 9 : Resultant eddy-current in the rotor bars for μ_r = 600 and s = 0.1 : (a) analytic and (b) FEM

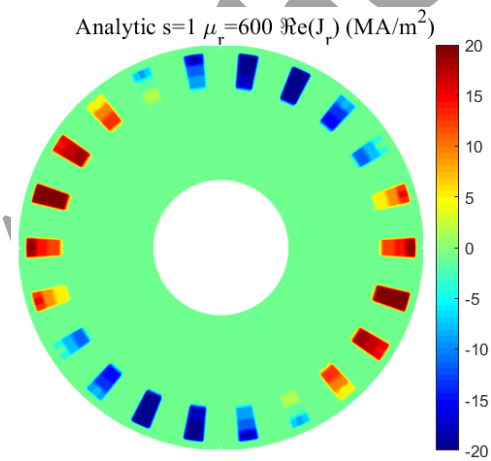

(a)

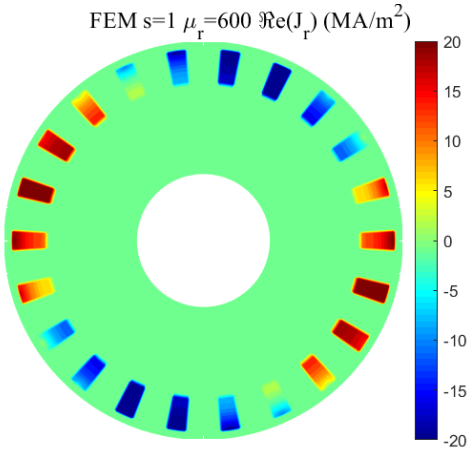

(b)

Figure 10 : Resultant eddy-current in the rotor bars for *μ_r = 600 and s = 1*: (a) analytic and (b) FEM

3.2. Nonlinear simulation results

In this section, the iron parts are considered to have nonlinear characteristic (i.e., 455 stainless steel). This characteristic is represented using the analytical model given in (Cale, et al., 2006). The *B*(*H*) curve and its parameters are provided in **Figure 11**. To determine the fundamental of the stator current, including its amplitude and phase shift, for the voltage supply, an EEC can be used (Roubache, et al., 2016).

Figure 12 shows the magnetic flux density in the middle of the air-gap with and without considering the magnetic saturation. The simulation is performed for $s = 1$ and $I_m = 70\ A$ to illustrate the impact of the magnetic saturation on the waveform of magnetic flux density**.** The relative permeability issued from the developed semi-analytical model is compared to that obtained by FEM (see **Figure 13**), showing good agreement.

Figure 14 illustrates the electromagnetic characteristics of the SCIM as a function of slip. It is observed that the results are consistent with those obtained by FEM for slip values below 0.1. However, at high slip values, the model gives an error of 5% to 10% between the analytical and numerical obtained currents. This error also extends to the electromagnetic torque results and is attributed to considering the eddy-currents induced in the rotor bars as constants.

The difference between the results obtained with and without considering the magnetic saturation is significant for high slip values. The explanation is that the increase in active current due to an increased load (or slip) saturates the magnetic circuit of the SCIM. This saturation results in a reduction of the machine's equivalent reactance, ultimately causing an increase in reactive current.

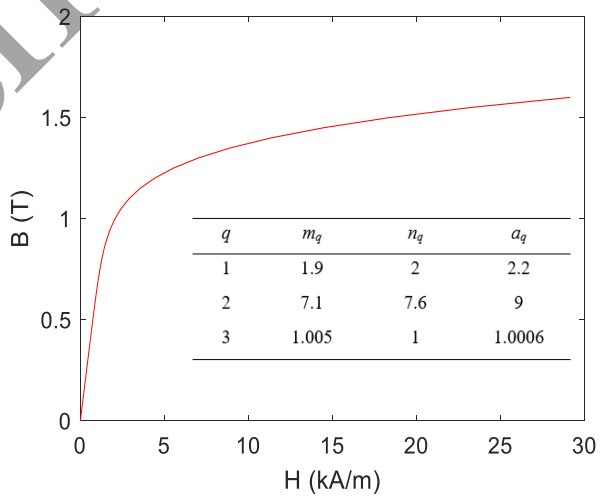

q	m_q	n_q	a_q
1	1.9	2	2.2
2	7.1	7.6	9
3	1.005	1	1.0006

Figure 11 : Parameters of *B(H)* curve according to the analytic model in (Cale et al., 2006)

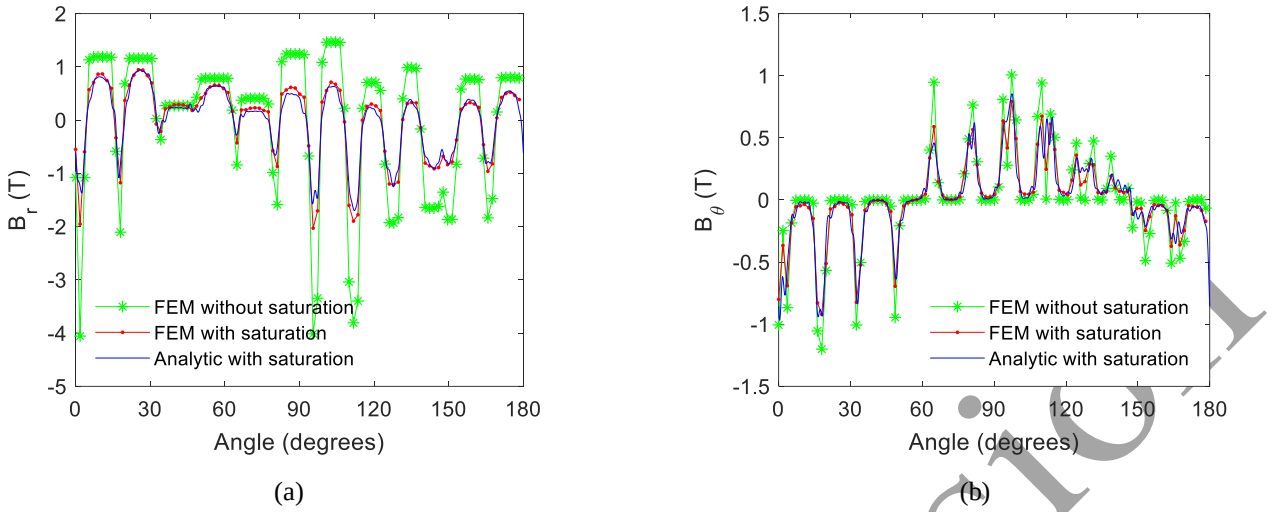

(a) (b)

Figure 12 : Waveform of *r*- and *θ*-component of B in the middle of the air-gap with and without saturation for s=1 and I = 70 A

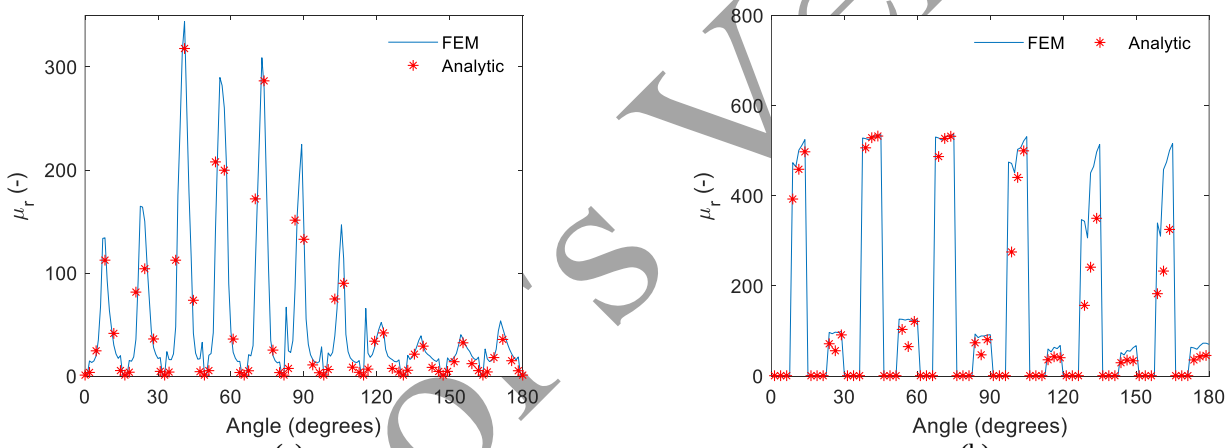

(a) (b)

Figure 13: Waveform of relative permeability at the radius: (a) (r2+Rr)/2 and (b) (r3+r4)/2 for s=1 and I = 70 A

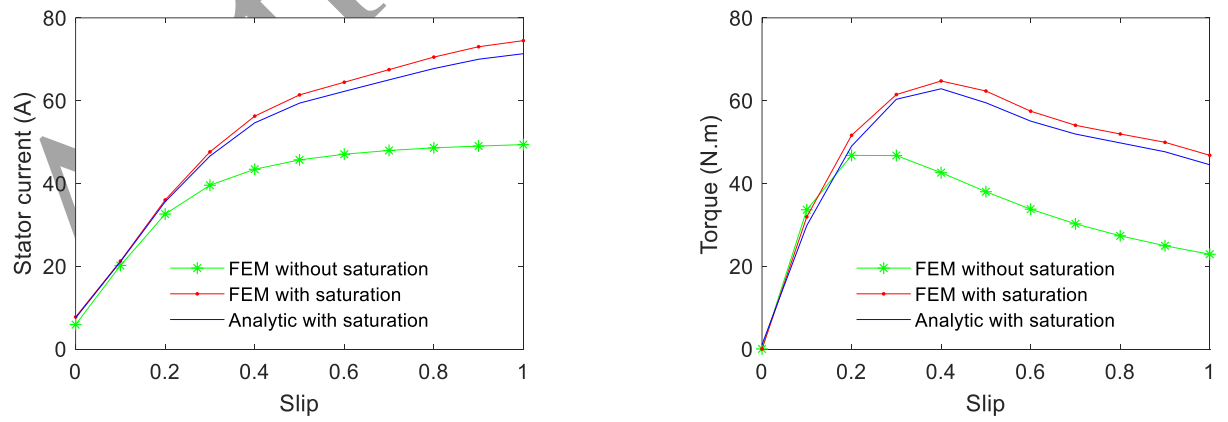

(a) (b)

Figure 14 : Electromagnetic characteristics of the SCIM with and without saturation as a function of slip: (a) Stator current and (b) Electromagnetic torque

Table 2 : Computation time, accuracy and size of the system

		Size of M	12,522	9,882	7,378	5,746	5,170
μ_r	s	Time (min)	3.1	1.56	0.62	0.31	0.23
100	0,1	$E_{\mathbf{B}}$ (%)	4.15	4.2	4.18	4.23	4.28
		E_{Γ} (%)	0.9	0.93	1.69	2.02	1.98
	1	$E_{\mathbf{B}}$ (%)	5.17	5.94	6.51	9.9	10.04
		E_{Γ} (%)	1.87	2.13	4.02	7.11	7.21
1000	0,1	$E_{\mathbf{B}}$ (%)	4.19	4.18	4.5	6.72	6.68
		E_{Γ} (%)	1.1	1.17	2.01	4.9	4.77
	1	$E_{\mathbf{B}}$ (%)	6.2	6.42	7.33	10.9	10.92
		E_{Γ} (%)	0.63	0.69	2.04	6.73	6.64

3.3. Model limitation – Size, accuracy and computation time

One essential aspect that needs addressing is the limitation of the semi-analytical model compared to the numerical model in terms of accuracy and computation time. It is evident that considering the harmonics of the eddy-currents induced in the rotor bars (Devillers, et al., 2018) for studying steady-state behavior at a given slip provides a significant advantage over the numerical model in terms of computation time, as the numerical model consumes considerable time in transient regime computations. However, a comparison between the proposed model and the magneto-harmonic numerical model has been conducted.

The accuracy of the developed model is directly related to the size of the E-SDs. This parameter can be evaluated in terms of the dimension of the linear system matrix M in **(33)**. **Table 2** represents the relative error between the semi-analytical and numerical models as a function of the size of matrix M and the computation time. The relative error is presented concerning the magnetic field in the middle of the air-gap and the electromagnetic torque. These errors are calculated as follows:

$$E_{\mathbf{B}}(\%) = \frac{RMS\left(\mathbf{B}_I^{Num} - \mathbf{B}_I^{Ana}\right)}{RMS\left(\mathbf{B}_I^{Num}\right)} \tag{43}$$

$$E_{\Gamma}(\%) = \frac{\left|\Gamma^{Num} - \Gamma^{Ana}\right|}{\left|\Gamma^{Num}\right|} \tag{44}$$

The numerical results of the magnetic field are calculated with 185,341 nodes and 369,262 elements, with a computation time of 2.26 minutes. **Table 2** demonstrates that the semi-analytical model provides good results for a high size of matrix M, but with a computation time comparable to that of FEM. However, for low values of slip (e.g., $s = 0{,}1$), where the magnetic vector potential exhibits minimal

distortion, it becomes possible to approximate by considering only one harmonic in the SDs-E without meshing the rotor and stator into very fine elements. In this case, the obtained error is approximately 6% for the magnetic field and 4% for the electromagnetic torque, with a significantly reduced computation time of less than 0.3 minutes.

4. CONCLUSION

In this paper, a semi-analytical model of SCIMs considering the local magnetic saturation effect and the eddy-currents induced in the rotor bars is presented. The developed modeling is based on the E-SDs technique, with the main assumption that the variation of the magnetic vector potential is not significant within the E-SDs. As a result, the eddy-currents in each E-SD belonging to the rotor bars are considered constant. These E-SDs are connected in both radial and tangential directions. The semi-analytical model has been validated for various values of slip and iron permeability with and without considering the magnetic saturation. The results are in good agreement with those obtained by FEM.

In cases where the magnetic vector potential is highly distorted, obtaining acceptable results requires meshing the rotor and stator into very fine E-SDs, which increases the computation time. Therefore, there is a need to optimize the implementation of this model, either by focusing on the optimal size of the E-SDs or by proposing solutions within the E-SDs that minimize the number of integration constants.

References

Aller, J. M. et al., 2013. *Model of the induction machine including saturation.* Lille, 15th European Conference on Power Electronics and Applications (EPE).

Boughrara, K., Dubas, F. & Ibtiouen, R., 2014. 2-D analytical prediction of eddy currents, circuit model parameters, and steady-state performances in solid rotor induction motors. *IEEE Transactions on Magnetics,* 50(12), pp. 1-14.

Cale, J., Sudhoff, S. D. & Turner, J., 2006. An improved magnetic characterization method for highly permeable materials. *IEEE Transactions on Magnetics,* 42(8), pp. 1974-1981.

Devillers, E. et al., 2016. *A review of subdomain modeling techniques in electrical machines: Performances and applications.* Lausanne, in Proc. ICEM.

Devillers, E. et al., 2018. An improved 2-D subdomain model of squirrel-cage induction machine including winding and slotting harmonics at steady state. *IEEE Transactions on Magnetics,* 54(2), pp. 1-12.

Dubas, F. & Boughrara, K., 2017a. New scientific contribution on the 2-D subdomain technique in Cartesian coordinates: Taking into account of iron parts. *Mathematical and Computational Applications,* 22(1), p. 17.

Dubas, F. & Boughrara, K., 2017b. New scientific contribution on the 2-D subdomain technique in polar coordinates: Taking into account of iron parts. *Mathematical and Computational Applications,* 22(4), p. 42.

Lubin, T., Mezani, S. & Rezzoug, A., 2011. Analytic calculation of eddy currents in the slots of electrical machines: Application to cage rotor induction motors. *IEEE Transactions on Magnetics,* 47(11), pp. 4650-4659.
Meeker, D. C., 2009. *Finite Element Method Magnetics ver. 4.2.*. [En ligne]
Available at: http://www.femm.info
Mollaeian, A. et al., 2021. Fourier-Based Modeling of an Induction Machine Considering the Finite Permeability and Nonlinear Magnetic Properties. *IEEE Transactions on Energy Conversion,* 36(4), p. 3427–3437.
Moulahoum, S., Touhami, O., Ibtiouen, R. & Fadel, M., 2007. *Induction machine modeling with saturation and series iron losses resistance.* Antalya, IEEE International Electric Machines & Drives Conference.
Roshandel, E., Mahmoudi, A., Kahourzade, S. & So, W., 2020. *Analytical Model and Performance Prediction of Induction Motors using Subdomain Technique.* Detroit, 2020 IEEE Energy Conversion Congress and Exposition (ECCE).
Roshandel, E., Mahmoudi, A., Kahourzade , S. & Soong, W. L., 2022. Saturation Consideration in Modeling of the Induction Machine Using Subdomain Technique to Predict Performance. *IEEE Transactions on Industry Applications,* 58(1), pp. 261-272.
Roubache, L., Boughrara, K., Dubas, F. & Ibtiouen, R., 2018. New subdomain technique for electromagnetic performances calculation in radial-flux electrical machines considering finite soft-magnetic material permeability. *IEEE Transactions on Magnetics,* 54(4), pp. 1-15.
Roubache, L., Boughrara, K., Dubas, F. & Ibtiouen, R., 2019. Elementary subdomain technique for magnetic field calculation in rotating electrical machines with local saturation effect. *COMPEL - The international journal for computation and mathematics in electrical and electronic engineering,* 38(1), pp. 24-45.
Roubache, L., Boughrara, K. & Ibtiouen, R., 2016. Analytical electromagnetic analysis of multi-phases cage rotor induction motors in healthy, broken bars and open phases conditions. *Progress In Electromagnetics Research B,* Volume 70, pp. 113-130.
Sapmaz, T. & Oner, Y., 2022. A novel hybrid model of electromagnetic performance for induction machine. *Electrical Engineering,* 104(5), p. 3381–3390.
Sprangers, R. L. J. et al., 2014. *Calculation of induced rotor current in induction motors using a slotted semi-analytical harmonic model.* Berlin, International Conference on Electrical Machines (ICEM).
Tiegna, H., Amara, Y. & Barakat, G., 2013. Overview of analytical models of permanent magnet electrical machines for analysis and design purposes. *Mathematics and Computers in Simulation,* Volume 90, pp. 162-177.
Tu, X., Dessaint, L., Champagne, R. & Al-Haddad, K., 2008. Transient modeling of squirrel-cage induction machine considering air-gap flux saturation harmonics. *IEEE Transactions on Industrial Electronics,* 55(7), pp. 2798-2809.